Cascaded metasurfaces enabling adaptive aberration corrections for focus scanning

Xiaotong Li, Xiaodong Cai, Chang Liu, Yeseul Kim, Trevon Badloe, Huanhuan Liu, Junsuk Rho and Shiyi Xiao

---

Related articles

Adaptive optics scanning laser ophthalmoscopy with two sources
Li Lingxiao, He Yi, Wang Yuanyuan, Wei Ling, Zhang Yudong
Opto-Electronic Engineering   2019 **46**, 180137   doi: 10.12086/oee.2019.180137

Application of hybrid modal algorithm in wavefront sensorless adaptive optics
Liu Wujie, Yuan Xiuhua, Zhou Zeyu, Li Qi, Zhao Ming
Opto-Electronic Engineering   2022 **49**, 220020   doi: 10.12086/oee.2022.220020

An optimized high-performance technique for adaptive optics static aberration correction
Ren Deqing, Zhang Tianyu, Wang Gang
Opto-Electronic Engineering   2022 **49**, 210319   doi: 10.12086/oee.2022.210319

A calibration method for Lyot filter
Wang Jia, Liu Yangyi, Rao Changhui
Opto-Electronic Engineering   2020 **47**, 190049   doi: 10.12086/oee.2020.190049

More related article in Opto-Electronic Journals Group website

Cascaded metasurfaces enabling adaptive aberration corrections for focus scanning

Xiaotong Li[1,2†], Xiaodong Cai[1†], Chang Liu[1†], Yeseul Kim[2],
Trevon Badloe[3], Huanhuan Liu[4], Junsuk Rho[2,5,6,7] and Shiyi Xiao[1*]

Scanning focused light with corrected aberrations holds great importance in high-precision optical systems. However, conventional optical systems, relying on additional dynamical correctors to eliminate scanning aberrations, inevitably result in undesired bulkiness and complexity. In this paper, we propose achieving adaptive aberration corrections coordinated with focus scanning by rotating only two cascaded transmissive metasurfaces. Each metasurface is carefully designed by searching for optimal phase-profile parameters of three coherently worked phase functions, allowing flexible control of both the longitudinal and lateral focal position to scan on any custom-designed curved surfaces. As proof-of-concept, we engineer and fabricate two all-silicon terahertz meta-devices capable of scanning the focal spot with adaptively corrected aberrations. Experimental results demonstrate that the first one dynamically scans the focal spot on a planar surface, achieving an average scanning aberration of 1.18% within the scanning range of ±30°. Meanwhile, the second meta-device scans two focal points on a planar surface and a conical surface with 2.5% and 4.6% scanning aberrations, respectively. Our work pioneers a breakthrough pathway enabling the development of high-precision yet compact optical devices across various practical domains.

Keywords: terahertz; focus scanning; aberration correction; dielectric metasurface

Introduction

Dynamic light focus control has attracted considerable attention for both scientific curiosity and important applications in many fields, such as bioimaging, laser processing, and optical tweezers. One critical challenge arises from scanning aberrations, i.e., the deviation of the focal position from the target surface, resulting in a significant decrease in focus quality (both intensity and shape) during light focus scanning, thereby constraining the dynamical precision of the optical scanning system[1,2]. Conventional techniques, which depend on additional

¹Key Laboratory of Specialty Fiber Optics and Optical Access Networks, Joint International Research Laboratory of Specialty Fiber Optics and Advanced Communication, Shanghai Institute for Advanced Communication and Data Science, Shanghai University, Shanghai 200240, China; ²Department of Mechanical Engineering, Pohang University of Science and Technology (POSTECH), Pohang 37673, Republic of Korea; ³Graduate School of Artificial Intelligence, Pohang University of Science and Technology (POSTECH), Pohang 37673, Republic of Korea; ⁴Shenzhen Institute of Advanced Technology, Chinese Academy of Sciences, Shenzhen 518055, China; ⁵Department of Chemical Engineering, Pohang University of Science and Technology (POSTECH), Pohang 37673, Republic of Korea; ⁶Department of Electrical Engineering, Pohang University of Science and Technology (POSTECH), Pohang 37673, Republic of Korea; ⁷POSCO-POSTECH-RIST Convergence Research Center for Flat Optics and Metaphotonics, Pohang 37673, Republic of Korea.
†These authors contributed equally to this work.
*Correspondence: SY Xiao, E-mail: phxiao@shu.edu.cn
Received: 17 April 2024; Accepted: 12 July 2024; Published online: 6 September 2024

optical components and external control algorithms to correct such scanning aberrations, are thereby inevitably bulky and inefficient, run counter to the trend of integrated and miniaturized systems.

In recent years, metasurfaces, constructed by planar microstructures (i.e., meta-atoms) with precisely engineered optical responses, have provided new opportunities for controlling focal spot with ultra-compact and highly efficient devices[3–13]. Specifically, tunable metasurfaces have successfully demonstrated the dynamic tuning of electromagnetic (EM) responses at each position by integrating active elements (such as PIN diodes, varactors, graphene, and semiconductors) into individual meta-atoms[14–28]. Armed with these capabilities, researchers have explored pathways to achieve aberration-free control of focus by dynamically generating local phase distributions tailored to desired target wavefronts[29]. Despite numbers of promising designs proposed for the microwave regime, practical high-performance meta-devices capable of eliminating scan aberrations in higher frequency bands (e.g., terahertz, infrared, and visible regimes) have yet to be reported. This limitation ultimately arises from the lack of highly efficient and suitable active materials for high-frequency tunable

meta-devices, limiting their capability to flexibly and efficiently manipulate optical wavefronts.

More recently, cascaded metasurfaces have emerged as an alternative approach for dynamically controlling EM waves and based on this method scientists have demonstrated many fascinating manipulation effects[30–39]. For example, an advanced LiDAR technology is reported to achieve large field of view and high framerate by cascading ultrafast low field of view deflectors and large area metasurfaces[35], and a dual metasurface system is proposed to realize the precisely dynamically control of the Airy beam by encoding a cubic phase profile and two off-axis Fresnel lens phase profiles across the two metasurfaces[39]. In contrast to tunable meta-devices using local-phase-tuning mechanisms, cascaded metasurfaces globally change their phase profiles by simply rotating different layers of metasurfaces, significantly simplifying the inherent complexity of conventional local control methods. Consequently, this approach provides a more streamlined, efficient, and economical solution for controlling EM wave. However, cascaded metasurfaces encounter substantial challenges in eliminating scanning aberrations or achieving other high-precision optical manipulations. This is primarily due to the inherent limitations
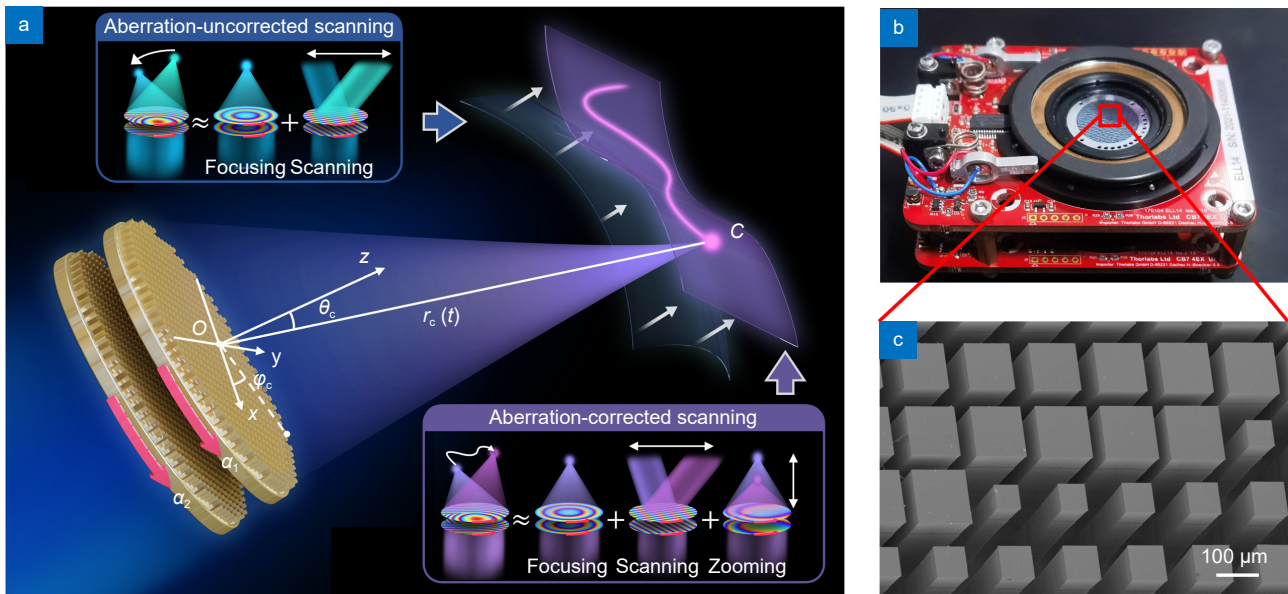
Fig. 1 | Schematic of the cascaded metasurfaces enabling adaptive aberration corrections for focus scanning. (**a**) Overview of cascaded metasurfaces, consisting of two layers of mechanically rotated transparent metasurfaces (with rotation angle α_1 and α_2, respectively), is capable of dynamically scanning the focal spot on the custom-designed aberration-corrected scanning surface (purple surface) compared to the aberration-uncorrected scanning surface (blue surface). Here, r_c represents the position of focal spot, and θ_c and φ_c represent the polar angle and azimuth angle of focal spot. Insets illustrate the intuitive physical picture of the typical origin of scanning aberrations, using hyperbolic scanning lenses an example (blue panel), and how to adaptively correct these scanning aberrations with the coherent interplay between three different phase functions (purple panel). (**b**) Photograph of fabricated meta-device with two-layer all-silicon metasurfaces fixed in a motorized rotation stage. (**c**) Scanning electron microscope (SEM) image of the fabricated metasurface samples.

of their global phase-tuning mechanism, making precise local modifications exceptionally difficult to cater to high-precision dynamic EM wave generations.

In this work, we propose employing two cascaded transparent metasurfaces to achieve adaptive aberration corrections coordinated with focus scanning. Such adaptive aberration correction is realized by simply rotating two cascaded metasurfaces with carefully designed phase distributions, without the necessity for any additional optical elements or external control algorithms. We develop a generic parameter-solving method to optimize phase-profile parameters for moving a focal spot on any custom-designed curved surface, resulting in enhanced focus quality (both intensity and shape) during scanning. To validate our concept, we engineer and fabricate two meta-devices operating at the terahertz frequency range. Experimental results demonstrate that the first meta-device dynamically scans the focal spot on a planar surface, achieving an average scanning aberration of 1.18% within the scanning range of ±30°, which is a 5.56-fold improvement compared with a hyperbolic scanning lens. Meanwhile, the second meta-device is demonstrated to scan two focal points on a planar surface and a conical surface, exhibiting 2.5% and 4.6% average scanning aberrations respectively. Our approach is generic enough to extend to the development of other high-precision optical devices for versatile purposes. For instance, this technology can enable laser etching complex structures on three-dimensional curved surfaces or trapping and manipulating particles along customizable three-dimensional trajectories.

Principle and design

As shown in Fig. 1(a), the proposed meta-device is formed by two layers of mechanically rotated transparent metasurfaces, where each layer exhibits a pre-designed phase distribution $\Phi_i(\boldsymbol{r}_i)$ and a rotation angle α_i ($i = 1, 2$). We assume that the i'th layer, consisting of a series of different meta-atoms, exhibits identical principal axes $(\hat{u}_i, \hat{v}_i, \hat{z})$, which become different from the laboratory axes $(\hat{x}, \hat{y}, \hat{z})$ as the i'th layer is rotating. The positions in the local and laboratory coordinate systems are respectively represented as $\boldsymbol{r}_i = (u_i, v_i, z)^{\mathrm{T}}$ and $\boldsymbol{r} = (x, y, z)^{\mathrm{T}}$, while these two different coordinate systems can be connected as $\boldsymbol{r}_i = \boldsymbol{S}_i(\alpha_i) \cdot \boldsymbol{r}$ with

$$\boldsymbol{S}_i(\alpha_i) = \begin{pmatrix} \cos\alpha_i & \sin\alpha_i & 0 \\ -\sin\alpha_i & \cos\alpha_i & 0 \\ 0 & 0 & 1 \end{pmatrix}$$ being the rotation

matrix. By independently rotating the two-layer metasurfaces, the total phase profile of the whole cascaded metasurfaces can be re-constructed as $\Phi_{\mathrm{tot}}(\alpha_1, \alpha_2, \boldsymbol{r}) = \sum_i \Phi_i(\boldsymbol{r}_i)$, which enables us to dynamically control the outgoing waves through changing two rotation angles $\{\alpha_1, \alpha_2\}$.

Suppose the time-dependent focus position during the scanning process is denoted as $\boldsymbol{r}_c(t) = (x_c(t), y_c(t), z_c(t))^{\mathrm{T}}$, with the subscript "c" representing the central position of the focal spot. The corresponding phase profile, denoted as $\Phi_{\mathrm{target}}(\boldsymbol{r}, t)$, for generating the target focal spot can be expressed as

$$\Phi_{\mathrm{target}}(\boldsymbol{r}, t) = -k_0 \left[|\boldsymbol{r} - \boldsymbol{r}_c(t)| - |\boldsymbol{r}_c(t)| \right], \quad (1)$$

where $k_0 = 2\pi/\lambda$ is the vacuum wave vector, and λ is the working wavelength. If it is possible to find appropriate rotation angles $\{\alpha_1, \alpha_2\}$ at any given moment to satisfy $\Phi_{\mathrm{tot}}(\alpha_1, \alpha_2, \boldsymbol{r}) = \Phi_{\mathrm{target}}(\boldsymbol{r}, t)$, the focal spot can be precisely controlled to scan on any pre-designed surface, thus optimizing focal quality (both intensity and shape) to minimize scanning aberrations.

Consequently, the design problem transforms into searching for appropriate Φ_1 and Φ_2 to generate the desired phase distribution $\Phi_{\mathrm{tot}}(\alpha_1, \alpha_2, \boldsymbol{r})$. However, it is highly nontrivial to achieve this target due to the significant degrees of freedom associated with the phase distributions $\Phi_i(\boldsymbol{r}_i)$ for each layer. Typically, brute-force optimization is required for such design, which is computationally resource-intensive and almost impossible to accomplish.

To render the design of $\Phi_i(\boldsymbol{r}_i)$ more feasible, we develop a top-down design approach by decomposing the phase profile of each layer into a linear combination of three approximated phase functions, as expressed by:

$$\Phi_i(\boldsymbol{r}_i) = \Phi_i^{\mathrm{lens}}(\boldsymbol{r}_i) + \Phi_i^{\mathrm{grad}}(\boldsymbol{r}_i) + \Phi_i^{\mathrm{moiré}}(\boldsymbol{r}_i), \quad (2)$$

where $\Phi_i^{\mathrm{lens}}(\boldsymbol{r}_i) = -k_0(\sqrt{u_i^2 + v_i^2 + F_0^2} - F_0)/2$ is a hyperbolic lensing phase function with F_0 representing the focal length, $\Phi_i^{\mathrm{grad}}(\boldsymbol{r}_i) = \xi_i v_i$ is a linear gradient phase function with $\xi_i = (-1)^{i-1}\xi_0 = (-1)^{i-1} 0.5 k_0$ denoting the linear phase gradient, and $\Phi_i^{\mathrm{moiré}}(\boldsymbol{r}_i) = (-1)^{i-1} \chi_0(u_i^2 + v_i^2) \bmod (\arg(u_i + \mathrm{j}v_i) + \varphi_i + \pi)$ is a moiré phase function, where the "mod" function confines the angle value to $(-\pi, \pi]$, χ_0, φ_i, and j are the radial phase gradient, initial spiral phase and the imaginary unit, respectively.

These three phase functions are approximations

derived from the expansion of the ideal phase profile in Eq. (1) under the paraxial approximations (see S1 of the Supplemental information). With these approximated phase functions, there is no longer a necessity for brute-force optimizations of phase distributions $\Phi_i(\boldsymbol{r}_i)$ for each local position. Instead, we simply utilize the phase-profile parameters $\boldsymbol{M} = \{F_0, \chi_0, \varphi_1, \varphi_2\}$ (where $\boldsymbol{M}$ denotes a phase-profile parameter space) to search for the optimal design, making the design process more feasible and convenient.

Before delving into the detailed parameters searching process, we present an intuitive physical picture of how these three decomposed phase functions (Φ_i^{lens}, Φ_i^{grad}, and $\Phi_i^{\mathrm{moiré}}$) collaboratively control the focal spot in a flexible manner. Illustrated in inset to Fig. 1(a), these three phase functions correspond to distinct wave-control operations: wave focusing, beam scanning, and focus zooming. The lensing phase function, Φ_i^{lens}, converges EM wave passing through the cascaded device (comprising only Φ_i^{lens} terms) into a single focal spot, with the focal length determined by the phase-profile parameter F_0. Simultaneously, a double-layer metasurfaces employing the linear gradient phase function, Φ_i^{grad}, imparts a tangential phase gradient $\boldsymbol{\xi}_{\mathrm{tot}} = \nabla\left[\sum_i \Phi_i^{\mathrm{grad}}(\boldsymbol{r}_i)\right] = \sum_i[\xi_i(-\sin\alpha_i\hat{x} + \cos\alpha_i\hat{y})]$ to the incident beam, enabling dynamic beam sweeping controlled by the rotation angles $\{\alpha_1, \alpha_2\}$.

By employing only these two phase functions (Φ_i^{lens} and Φ_i^{grad}), a cascaded meta-device already demonstrates the capability to scan a focal spot controlled by the rotation angles $\{\alpha_1, \alpha_2\}$ [blue panel in Fig. 1(a)]. However, due to the constant focal length (F_0) in the lensing phase function, the focal spot scanning process inevitably induces a longitudinal displacement of the focal position $\Delta z_c = F_0(1 - \cos(\Delta\alpha))$ (see S2 of the Supplemental information), where $\Delta\alpha = (\alpha_2 - \alpha_1)/2$, while scanning the lateral position (x_c, y_c), resulting in a curved scanning surface $z_c = F_0\cos(\Delta\alpha)$ as depicted in Fig. 1(a) (see S7 of the Supplemental information). Such a curved scanning surface not only represents scanning aberrations that need to be corrected but is also equivalent to the off-axis scanning aberrations commonly observed in conventional scanning systems, such as hyperbolic scanning lenses (see S7 of the Supplementary information) or other optical systems. Conventionally, correcting scanning aberrations by eliminating the displacement between the focal point and the target scanning surface requires additional

optical components and external control algorithms[1,2].

To simplify such complex scanning systems, we propose integrating the moiré phase function, $\Phi_i^{\mathrm{moiré}}$, into the scanning system. As illustrated in the purple panel in Fig. 1(a), the double-layer cascaded $\Phi_i^{\mathrm{moiré}}$ is capable of generating quadratic phase profiles with a tunable focal length $F_{\mathrm{moiré}} = k_0/4\chi_0(\Delta\varphi + \Delta\alpha)$, where $\Delta\varphi = (\varphi_2 - \varphi_1)/2$ (see S3 of the Supplementary information). This suggests that the rotation of the cascaded moiré phase functions enables longitudinal position control of the focal spot. By incorporating $\Phi_i^{\mathrm{moiré}}$ into the original Φ_i^{lens} and Φ_i^{grad} phase profiles, it becomes possible to use the cascaded moiré phase to compensate for the longitudinal displacement induced by the Φ_i^{lens} and Φ_i^{grad} terms, leads to the achievement of adaptive aberration-corrected planar scanning. Furthermore, with a more carefully designed $\{\alpha_1, \alpha_2\}$ dependence of the cascaded moiré phase functions, it enables flexible control of both the longitudinal and lateral position simultaneously, which indicates a more sophisticated dynamic focal spot manipulation flexibility as illustrated in Fig. 1(a).

Notably, the integration of $\Phi_i^{\mathrm{moiré}}$ does not necessitate extra layers of cascaded metasurfaces. Instead, $\Phi_i^{\mathrm{moiré}}$ can be imparted into the existing two layers of metasurfaces. This approach allows the three decomposed phase functions (Φ_i^{lens}, Φ_i^{grad} and $\Phi_i^{\mathrm{moiré}}$) to collaboratively work together, enabling flexible focal spot scanning in a manner predetermined by the implanted phase-profile parameters $\{F_0, \chi_0, \varphi_1, \varphi_2\}$. Unfortunately, the process of determining these phase-profile parameters for specific scanning surfaces involves transcendental equations, rendering rigorous analytical solutions unattainable.

In the following sections, we develop a versatile optimization algorithm designed to determine optimal phase-profile parameters applicable to various scanning surfaces. Based on this design strategy, we proceed to demonstrate two meta-devices, both capable of scanning focal spots across pre-designed scanning surfaces [see the photograph of fabricated meta-device in Fig. 1(b) and 1(c)].

Result and discussion

Meta-device for adaptively corrected planar scanning

Our first design target is to develop an adaptively corrected planar scanner (scanning the focal spot on a transverse planar surface), with the aim of maximizing the focus quality on the planar surface. This planar scanning

surface is expressed as

$$z_c(\alpha_1, \alpha_2) \approx h \,, \qquad (3)$$

where the lateral focal position (x_c, y_c) can be dynamically controlled by the rotation angles $\{\alpha_1, \alpha_2\}$, and h is a pre-determined constant representing the longitudinal focal position of the scanning surface as depicted in Fig. 2(a). For simplicity and without loss of generality, we set parameters as $h = 4$ mm and $\varphi_1 = -\varphi_2 = \varphi_0$ to demonstrate the functionalities of our meta-device. Consequently, the original parameter space $\boldsymbol{M} = \{F_0, \chi_0, \varphi_1, \varphi_2\}$ can be simplified into a reduced parameter space $\boldsymbol{M}' = \{F_0, \chi_0, \varphi_0\}$.

As the initial step, we solve $\Phi_{tot}(\alpha_1, \alpha_2, \boldsymbol{r}) = \Phi_{target}(\boldsymbol{r}, \boldsymbol{r}_c)$ to establish the relationship between the phase-profile parameters $\{F_0, \chi_0, \varphi_0\}$ and focal spot $\boldsymbol{r}_c$ for different rotation angles $\{\alpha_1, \alpha_2\}$. However, there is ambiguity in solving this phase-matching

equation, as the total phase distribution of metalens $(\Phi_{tot}(\alpha_1, \alpha_2, \boldsymbol{r}))$ typically comprises two discontinuous phase regions (Region I and Region II) as depicted in Fig. 2(b). These two regions correspond to two different focusing phases, commonly observed in a moiré lens. This phenomenon arises from the fact that a clockwise rotation within the moiré phase profile is indistinguishable from a counterclockwise rotation, leading to an ambiguity into the phase distributions of the moiré lens[30,31]. Here, we designate Region I as the operational area, while Region II is considered as residual one. This strategy inevitably impacts the operational efficiency of our meta-device, as it reduces the working region (Region I) during scanning, posing a trade-off for correcting aberrations using our approach.

Based on the selected operational area, we derive the $\boldsymbol{r}_c \sim \{F_0, \chi_0, \varphi_0\}$ relationship, expressed as
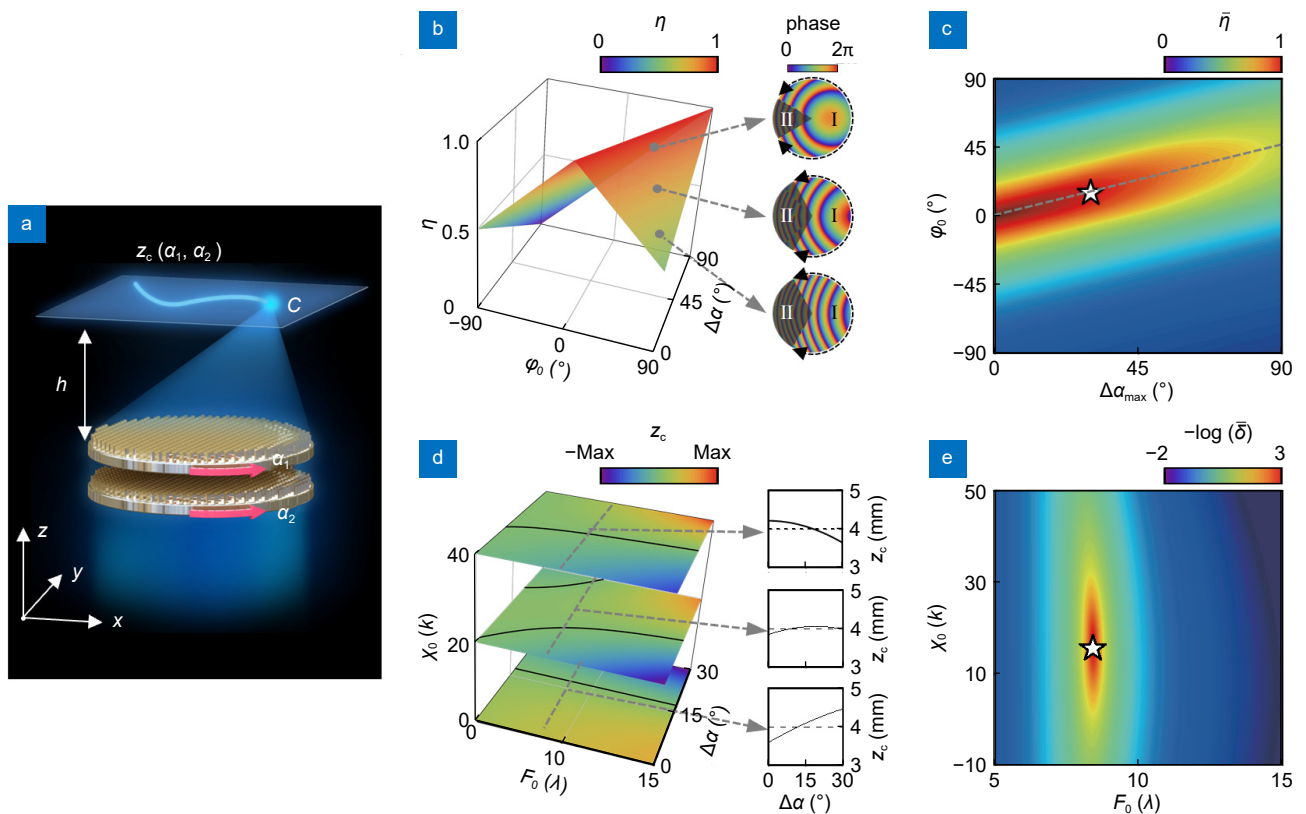
Fig. 2 | Searching algorithm for optimal phase-profile parameters. (**a**) Schematic of meta-device for adaptively corrected planar scanning. (**b**) The theoretical working efficiency η varies with φ_0 and $\Delta\alpha$, where the total phase profiles $\Phi_{tot}(\alpha_1, \alpha_2, \boldsymbol{r})$ for different rotation angle $\{\alpha_1, \alpha_2\}$ are depicted as the right panel. (**c**) The average working efficiency $\bar{\eta}$ varies with $\Delta\alpha_{max}$ and φ_0, where the dashed grey line represents the optimized $\bar{\eta}$ with varying $\Delta\alpha_{max}$, and the star symbol is the selected parameters ($\varphi_0 = 15°$) to balance the scanning range ($\Delta\alpha_{max} = 30°$) and efficiency. (**d**) The longitudinal focal position z_c varies with F_0, χ_0 and $\Delta\alpha$ for fixed φ_0, where $z_c \sim \Delta\alpha$ dependence for different values of F_0 and χ_0 are depicted in the right panel. (**e**) The average scanning aberration $\bar{\delta}$ varies with F_0 and χ_0 with the star symbol denoting the optimal chosen ($F_0 = 8.4\lambda$, $\chi_0 = 16.3k_0$, $\varphi_0 = 15°$).

$$\begin{cases} x_c\left(\Delta\alpha, \alpha_{\mathrm{av}}\right) = \sin\left(\Delta\alpha\right)\cos\left(\alpha_{\mathrm{av}}\right) R_c\left(F_0, \chi_0, \varphi_0, \Delta\alpha\right) \\ y_c\left(\Delta\alpha, \alpha_{\mathrm{av}}\right) = \sin\left(\Delta\alpha\right)\sin\left(\alpha_{\mathrm{av}}\right) R_c\left(F_0, \chi_0, \varphi_0, \Delta\alpha\right) \\ z_c\left(\Delta\alpha\right) = \cos\left(\Delta\alpha\right) R_c\left(F_0, \chi_0, \varphi_0, \Delta\alpha\right) \end{cases},$$

(4)

where $R_c\left(F_0, \chi_0, \varphi_0, \Delta\alpha\right) = k_0 F_0/[k_0 - 4\chi_0 F_0\left(\Delta\alpha + \varphi_0\right)]$ represents the distance between the focal spot and the center of the meta-device, $\Delta\alpha = (\alpha_2 - \alpha_1)/2$ denotes the average rotation angle difference, and $\alpha_{\mathrm{av}} = (\alpha_1 + \alpha_2)/2$ denotes the average rotation angle, respectively.

Examining Eq. (4), we observe that the scanning surface exhibits rotational symmetry, with the polar and azimuthal angles of the scanning focus represented by $\Delta\alpha$ and α_{av}, respectively. This implies that changing α_{av} enables the focal point to move along rotational direction on the scanning surface, while changing $\Delta\alpha$ only drive the focal point to move radially on this surface. On the other hand, only $\Delta\alpha \sim z_c$ dependence of the focal spot needs to be considered while determining the shape of scanning surface, also due to the presence of rotational symmetry. Thus, achieving planar scanning of the focal point transforms into the quest for suitable parameters $\{F_0, \chi_0, \varphi_0\}$ ensuring $z_c\left(\Delta\alpha\right) \approx h$ consistently. Unfortunately, this problem cannot be rigorously solved due to the complicated dependence between $\Delta\alpha$ and z_c.

To address this issue, we numerically investigate the $z_c \sim \Delta\alpha$ dependence by employing a Taylor series expansion to express z_c near $\Delta\alpha = 0$, expressed as

$$z_c\left(\Delta\alpha\right) \approx f_0 + f_1\Delta\alpha + f_2(\Delta\alpha)^2,$$

(5)

where $f_0 = z_c(0)$, $f_1 = \partial z_c/\partial(\Delta\alpha)|_{\Delta\alpha=0}$ and $f_2 = (1/2)\partial^2 z_c/\partial(\Delta\alpha)^2|_{\Delta\alpha=0}$ represent the coefficients for zeroth-order, first-order and second-order derivative terms, respectively. According to Eq. (5), achieving precise planar scanning requires all coefficients of high-order derivative terms to be simultaneously zero, i.e., $f_1 = f_2 = 0$. However, this condition almost impossible to satisfy in general cases, making it challenging to achieve perfect planar scanning.

We alternatively seek the optimal solution to approximate the desired $z_c \sim \Delta\alpha$ dependence by considering the overall effects of all the higher-order terms in Eq. (5). Initially, we set the average longitudinal focal position $\bar{z}_c$ equal to the pre-defined target value h, expressed as $f_0 + (1/2)f_1\Delta\alpha_{\mathrm{max}} + (1/3)f_2(\Delta\alpha_{\mathrm{max}})^2 = h$, where $\Delta\alpha_{\mathrm{max}}$ is the maximum scanning polar angle in our design ($\Delta\alpha \in [0°, \Delta\alpha_{\mathrm{max}}]$). This equation serves as a constraint in the process of seeking the optimal solution, refining

the search range within the parameter space M'. Additionally, we define the scanning range of our proposed meta-device as the range of scanning angles of the polar angle, denoted as $\pm\Delta\alpha_{\mathrm{max}}$, due to the rotational symmetry of the scanning surface.

To further determine the optimal phase-profile parameters, two figures of merit (FOMs) must be taken into considerations. As depicted in Fig. 2(b), we define the theoretical working efficiency η as

$$\eta = 1 - \frac{|\Delta\alpha - \varphi_0|}{\pi},$$

(6)

to describe the proportion of operational area during scanning. Figure 2(b) illustrates that η reaches its maximum value only at $\Delta\alpha = \varphi_0$, indicating that the operational area coincides with the entire metasurface, and the theoretical efficiency of the meta-device reaches 1 only under this condition. When $\Delta\alpha \neq \varphi_0$, the operational area unavoidably decreases, means that η cannot consistently maintain its maximum value within the scanning range. Hence, we design the average value of the theoretical working efficiency $\bar{\eta} = \int_0^{\Delta\alpha_{\mathrm{max}}} \eta\mathrm{d}\Delta\alpha/\Delta\alpha_{\mathrm{max}}$ to be maximized.

Figure 2(c) illustrates how $\bar{\eta}$ varies with changing $\Delta\alpha_{\mathrm{max}}$ and φ_0, exhibiting the optimal $\bar{\eta}$ located at $\Delta\alpha_{\mathrm{max}} = 2\varphi_0$, indicating the existence of an optimized solution $\varphi_0 = (1/2)\Delta\alpha_{\mathrm{max}}$ for any $\Delta\alpha_{\mathrm{max}}$ such that the average working efficiency reaches its maximum value. Although an optimal solution is found for different $\Delta\alpha_{\mathrm{max}}$, it is crucial to note that as $\Delta\alpha_{\mathrm{max}}$ increases, the optimal $\bar{\eta}$ inevitably decreases (due to η decreases with increasing $|\Delta\alpha - \varphi_0|$). This provides a quantitative illustration of the previously discussed trade-off between scanning range and efficiency in our proposed aberration correction approach. In this design, we choose $\Delta\alpha_{\mathrm{max}} = 30°$ and $\varphi_0 = 15°$ [see star symbol in Fig. 2(c)] to strike a balance between the scanning range and the working efficiency of the meta-device.

Having determined φ_0, we proceed to search for the other two parameters $\{F_0, \chi_0\}$. Figure 2(d) illustrates how the $\Delta\alpha \sim z_c$ dependence varies as a function of F_0 and χ_0, demonstrating that a proper choice of $\{F_0, \chi_0\}$ capable of minimizing the deviation (i.e. scanning aberration) between z_c and h throughout the scanning process. To quantitatively determine $\{F_0, \chi_0\}$ parameters, we define the average scanning aberration as:

$$\overline{\delta} = \left(\frac{1}{\Delta\alpha_{\max}} \right) \sqrt{\int_0^{\Delta\alpha_{\max}} \left(\frac{z_c(\Delta\alpha)}{\overline{z}_c} - 1 \right)^2 \mathrm{d}(\Delta\alpha)} . \quad (7)$$

Figure 2(e) plots the phase diagram of $\overline{\delta}$ as F_0 and χ_0 change, revealing that $\overline{\delta}$ reaches its minimum value only at $F_0 = 8.4\lambda$ and $\chi_0 = 16.3k_0$. This solution corresponds to the middle inset in Fig. 2(d), where the longitudinal focal coordinate z_c closely aligns with the target value h with two intersections, resulting in significantly smaller deviations compared to other cases.

Through these processes, all required optimal parameters $\{F_0, \chi_0, \varphi_0\}$ are obtained for planar aberration correction. By further inserting optimal $\{F_0, \chi_0, \varphi_0\}$ into Eq. (2), the phase profiles Φ_i of each layer metasurface are finally calculated as depicted in the insets of Fig. 3(a).

We engineer, fabricate, and characterize this meta-device in the terahertz regime. Before presenting the simulated and measured results, we employ the standard Green's function approach to illustrate the adaptive aberration correction capability (see S7 of the Supplementary information). As shown in Fig. 3(b), theoretical results indicate that the adaptively corrected planar scanner maintains the longitudinal position of the focus near the target value h throughout the scanning process. In comparison, the scanning aberration of a hyperbolic scanning lens continues to significantly increase with the increment of $\Delta\alpha$ and reaches its maximum value at $\Delta\alpha_{\max}$. Quantitative analysis results demonstrate our proposed adaptively corrected planar scanner reduces the average scanning aberration (ξ) by a factor 6.2 (reducing from 5.82% to 0.94%), particularly achieving a 12-fold improvement of scanning aberration at the maximum scanning angle $\Delta\alpha_{\max}$ (reducing from 15% to 1.25%), compared with a hyperbolic scanning lens.

Since the inevitable ohmic loss of metals at high frequencies[11,40], we employ all-silicon metasurfaces to build our meta-device, operating at a frequency of 0.6 THz, to achieve desired phase profiles while maintain high transmittance. Our design consists of a single-layer metasurface with square-shaped top silicon posts and uniform-sized bottom silicon posts deposited on opposite sides of a continuous silicon spacer [see Fig. 1(c) and S4 of the Supplementary information]. The top silicon posts vary in size to generate the desired phase profile, as depicted in the inset of Fig. 3(a). Meanwhile, the bottom posts, maintaining a uniform size, function as an anti-reflection layer to ensure high transmissive efficiency (see S4 of the Supplementary information). Utilizing these fabri-cated samples, we stack two layers of metasurface along the z-direction, affixed on a motorized rotation stage (see S6 of the Supplementary information), as schematically shown in Fig. 3(a). The diameter of normal incident terahertz wave is 7 mm and the numerical aperture (NA) of meta-device is 0.66. The diameter of metasurface is 22 mm to match the motorized rotation stage. The spacing distance between the cascaded metasurfaces is 300 μm (approximately 0.6λ) considering the practical realization in experiments and the interlayer coupling of the cascaded metasurfaces[41] (see S5 of the Supplementary information).

Using a normally incident linear polarized (LP) beam ($E \parallel \hat{x}$), we illuminate the meta-device and employ a terahertz near-field scanning system to measure the electric field distributions on both the vertical plane (with $y = 0$ mm) and horizontal plane (with $z = 4$ mm) while increasing $\Delta\alpha$. In Fig. 3(c) and 3(d), the measured and simulated electric intensity distributions are depicted at the operational frequency of 0.6 THz. Clearly, the incident waves have been well-focused to the pre-determined center point of $z = 4$ mm plane after passing through meta-device at $\Delta\alpha = 0°$. As the rotation angles $\Delta\alpha$ increase, the focal position [illustrated by dotted lines in Fig. 3(c)] dynamically moves along the x-direction, maintaining an almost uniform transverse plane around $z = 4$ mm. Furthermore, we evaluate the FWHM in Fig. 3(c) and 3(d) to characterize the device's performance. The experimental/simulated FWHM values for $\Delta\alpha = 0°, 10°, 20°, 30°$ are 0.45/0.42 mm, 0.51/0.46 mm, 0.56/0.52 mm, 0.93/0.60 mm, respectively, closely approaching the diffraction limit. We also define the focusing efficiency as the ratio of the focal intensity captured at the focal spot to the amount of incident EM wave entering the meta-device. The focusing efficiencies at $\Delta\alpha = 0°, 10°, 20°, 30°$ are 23.2%/30.2%, 25.1%/33.1%, 24.5%/30.8%, and 23.7%/31.0%, respectively, in experimental and simulated results. To demonstrate the polarization insensitivity of the proposed strategy we also collect the experimental intensity distribution above the meta-device with y-polarized incidence (see S9 of the Supplemental information).

All experimental results are in good agreement with theoretical predictions, validating the effectiveness of our proposed meta-device in controlling focal spots. The device exhibits an average scanning aberration of approximately 1.18% within the scanning range of ±30°, with a scanning aberration of 1.5% at the maximum scanning
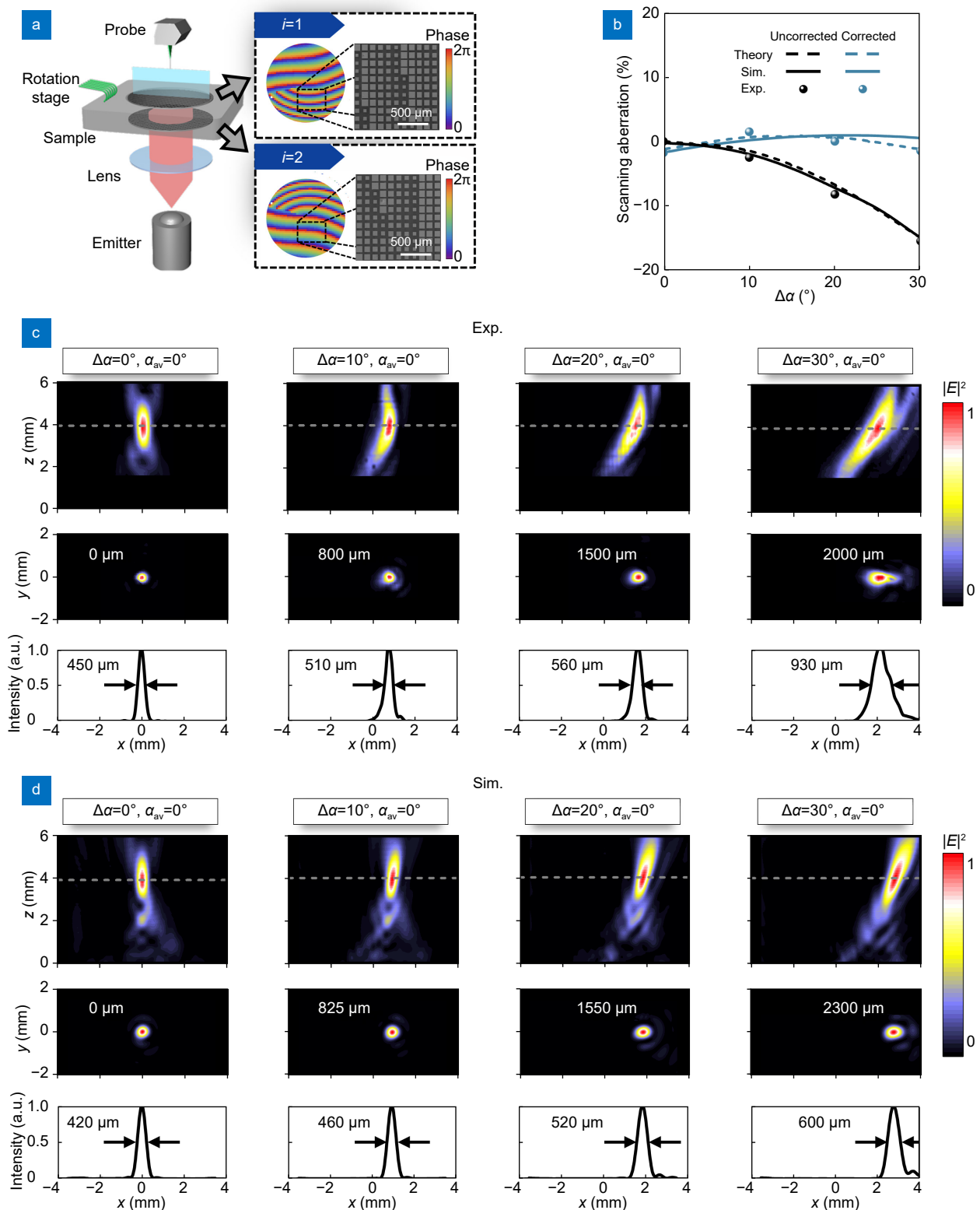
Fig. 3 | The experimental setup and terahertz characteristics of the meta-device for adaptively corrected planar scanning. (**a**) Schematics of the experimental setup, with the theoretical phase profiles and the top view SEM of each layer in the right. (**b**) Theoretical (dashed), simulated (solid) and experimental (dotted) results of longitudinal focal position for adaptively corrected planar scanner (blue) compared with hyperbolic scanning lenses (black). Experimental (**c**) and simulated (**d**) intensity distributions on *xz*-plane (top) and *xy*-plane (middle) corresponding to different $\Delta\alpha$, and the intensity profiles along the diameter (bottom) at the focal plane with the full width at half maximum (FWHM) marked. Here, the grey dashed lines in (c) and (d) represent the position of the maximum intensity of focal spot.

angle. Compared to hyperbolic scanning lenses, the performance of our proposed meta-device has increased by an average factor of 5.56 within the scanning range, and by a factor of 10.33 at the maximum scanning angle. To further illustrate the improvement of the quality of focal spots, we present the focus intensity and shape with varying scanning angles, revealing an 18% enhancement of focus intensity and a notable improvement in the shape of the focal spots (see S7 of the Supplemental information). Certainly, such meta-device can also control the focal spot to move along a continuous curve on the customized scanning surface, such as an S-shaped scanning trajectory (see S8 of the Supplementary information). Additionally, through the selection of appropriate parameters, our proposed design strategy can further control focal intensity during the scanning process (see S11 of the Supplementary information), which holds significant promise for improving the large-area uniformity in applications such as laser cladding and laser hard-

ening. We also note that slight discrepancies between the simulated and measured results may arise due to fabrication tolerances and couplings between the two layers of metasurfaces.

Meta-device for adaptively corrected dual-focus scanning

Our scheme is generic enough that it can also be extended to achieve more complicated focus scanning. As an illustration, we develop an adaptively corrected dual-focus scanner with the first focal spot scanning within a planar surface [the same scanning surface shown in Fig. 2(a)], and the second focal spot scanning within a conical surface, both schematically depicted in Fig. 4(a). We employ these two scanning surfaces as illustrations, emphasizing that the concept can be readily extended to more sophisticated curved surfaces, which has potential applications in optical tweezers and laser processing[7,13].

The parametric equations governing these two
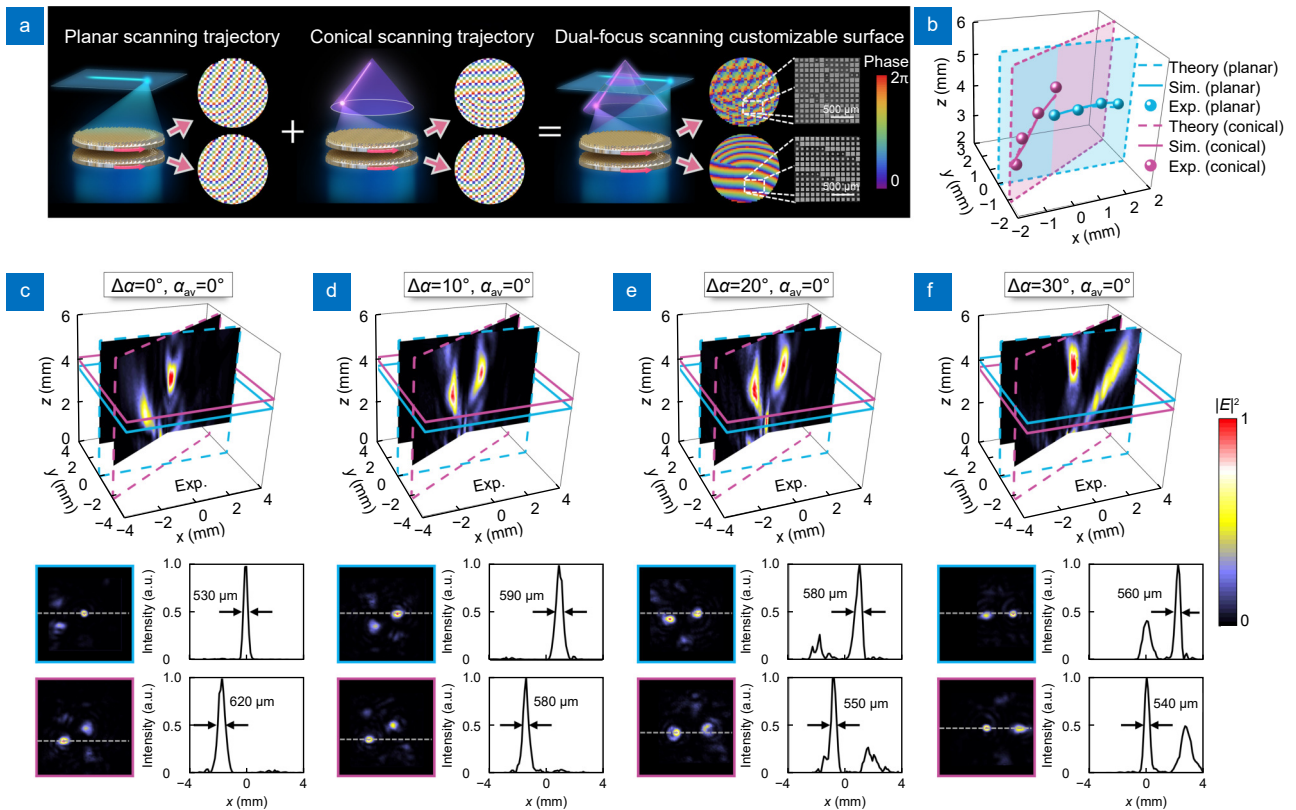
Fig. 4 | Terahertz characteristics of the adaptively corrected dual-focus scanner. (**a**) Design strategy of the meta-device for scanning two focal spots in different scanning surfaces, with the theoretical phase profiles and the top view SEM of each layer in the right. (**b**) Theoretical (dashed), simulated (solid) and experimental (dotted) results of the position for focal spot *A* (blue) and *B* (pink) of the adaptively corrected dual-focus scanner. The blue plane and pink plane are two vertical planes at the azimuthal angle 0° and 30°. (**c**–**f**) Experimental intensity distributions on two vertical planes (top) for two focal spots at the azimuthal angle 0° (dashed blue) and 30° (dashed pink) corresponding to different Δα, with two horizontal planes (bottom left) at focal plane for focal spot *A* (solid blue) and *B* (solid pink). The intensity profiles along the diameter (bottom right) at the focal plane with the FWHM marked.

scanning surfaces are expressed as follows:

$$
\begin{cases}
z_A\left(\Delta\alpha, \alpha_{\mathrm{av}}\right) = h_A \\
z_B\left(\Delta\alpha, \alpha_{\mathrm{av}}\right) + l_B r_B\left(\Delta\alpha, \alpha_{\mathrm{av}}\right) = h_B
\end{cases}, \quad (8)
$$

where the subscript "A" and "B" labels the two focal spots, $r_B\left(\Delta\alpha, \alpha_{\mathrm{av}}\right) = \sqrt{x_B^2\left(\Delta\alpha, \alpha_{\mathrm{av}}\right) + y_B^2\left(\Delta\alpha, \alpha_{\mathrm{av}}\right)}$, $h_A = 4$ mm, $l_B = 0.58$ and $h_B = 4.65$ mm represent predetermined constants defining the geometric parameters for these scanning surfaces. As discussed earlier, achieving the scanning of these two focal spots along the different surfaces (as described in Eq. (8)) requires determining two sets of optimal design parameters in parameters spaces $\boldsymbol{M}_A = \left\{\xi_{0,A}, F_{0,A}, \chi_{0,A}, \varphi_{i,A}\right\}$ and $\boldsymbol{M}_B = \left\{\xi_{0,B}, F_{0,B}, \chi_{0,B}, \varphi_{i,B}\right\}$. Realizing such a meta-device poses two primary challenges: (i) generating two independent focal points within a single device and (ii) enabling independent scanning surfaces for these two focal spots.

We start with presenting how to independently design two focal spots in our proposed meta-device. To achieve this, we employ a "multiplexing" strategy as illustrated in Fig. 4(a). In this meta-device, the phase distribution of the first layer ($i = 1$) is partitioned into two segments: Subsection A [represented as the planar scanning in Fig. 4(a)] and Subsection B [represented as the conical scanning in Fig. 4(a)], utilizing a checkerboard pattern distribution. By further cascading this checkerboard phase distribution with a second layer [as depicted in Fig. 4(a)], we are able to control two focal spots along their own trajectories on different scanning surface. Consequently, this strategy empowers the two independently designed focal spots to scan along their own surfaces.

Following this, we proceed to design the phase distribution of each layer to achieve the desired scanning surfaces for the two focal spots. Based on last section, our parameter searching method holds theoretical applicability to any scanning surface. Employing a similar approach, we employ two reduced parameter spaces, i.e., $\boldsymbol{M}'_A = \{F_0, \chi_0, \Delta\varphi_{0,A}\}$ and $\boldsymbol{M}'_B = \{F_0, \chi_0, \Delta\varphi_{0,B}\}$, for two respective focal spots (see S12 of the Supplemental Material). Based on the reduced parameter spaces, we obtain the position of the two focal spots respectively as a function of the rotation angle of metasurface:

For the focus A,

$$
\begin{cases}
x_A\left(\Delta\alpha, \alpha_{\mathrm{av}}\right) = \sin\left(\Delta\alpha\right)\cos\left(\alpha_{\mathrm{av}}\right) R\left(\Delta\alpha\right) \\
y_A\left(\Delta\alpha, \alpha_{\mathrm{av}}\right) = \sin\left(\Delta\alpha\right)\sin\left(\alpha_{\mathrm{av}}\right) R\left(\Delta\alpha\right) \\
z_A\left(\Delta\alpha\right) = \cos\left(\Delta\alpha\right) R\left(\Delta\alpha\right)
\end{cases}, \quad (9)
$$

For the focus B,

$$
\begin{cases}
x_B\left(\Delta\alpha, \alpha_{\mathrm{av}}\right) = \sin\left(\Delta\alpha - \gamma\right)\cos\left(\alpha_{\mathrm{av}} + \gamma\right) R\left(\Delta\alpha - \gamma\right) \\
y_B\left(\Delta\alpha, \alpha_{\mathrm{av}}\right) = \sin\left(\Delta\alpha - \gamma\right)\sin\left(\alpha_{\mathrm{av}} + \gamma\right) R\left(\Delta\alpha - \gamma\right) \\
z_B\left(\Delta\alpha\right) = \cos\left(\Delta\alpha - \gamma\right) R\left(\Delta\alpha - \gamma\right)
\end{cases}, \quad (10)
$$

where $\Delta\alpha$, α_{av} and $R\left(\Delta\alpha\right)$ are defined in Eq. (4) and $\gamma = 30°$ determines the initial polar and azimuth angles of the focus B. Subsequently, we employ similar FOMs as described by Eq. (6) and Eq. (7) to determine the optimal design parameters (see S12 of the Supplemental Material). Similar to the previous design, we utilize the standard Green's function approach to verify the aberration correction capability of adaptively corrected dual-focus scanner (see S12 of the Supplemental Material). Computational results demonstrate that throughout the entire scanning process, the average scanning aberrations of our proposed dual-focus scanner are around 1.5% and 3.8%, confirming the effectiveness of the design.

Finally, we followed the design and fabrication procedures described in the first design to produce samples, as depicted in Fig. 4(a). With these fabricated samples, we conducted experimental measurements on the two focal spots as increasing two rotating angles α_1 and α_2. The results of the position for focal spot A (blue) and B (pink) of the adaptively corrected dual-focus scanner are shown in Fig. 4(b). The measured electric field distributions on two vertical planes for two focal spots, with azimuthal angle 0° [dashed blue plane in Fig. 4(c–f)] and 30° [dashed pink plane in Fig. 4(c–f)], and two horizontal planes, with $z = 4$ mm [solid blue plane in Fig. 4(c–f)] and $z = \cos\left(\Delta\alpha - 30°\right) R\left(\Delta\alpha - 30°\right)$ [solid pink plane in Fig. 4(c–f)], respectively. As the rotation angle $\Delta\alpha$ increase, the measured focal positions precisely matched the theoretical predictions. Focal spot A, positioned at an azimuthal angle of 0°, dynamically scans within a single horizontal plane at $z = 4$ mm. Meanwhile, focal spot B, at an azimuthal angle of 30°, undergoes simultaneous dynamic scanning with increased horizontal and vertical coordinates. Such focal scanning behavior is clearly observable in the measure field intensity on the targeted $z = 4$ mm plane and the experimental FWHM for the two focal spots while rotating two layers of metasurfaces, as illustrated in Fig. 4(c–f). As a comparison, we also present simulated results for two focal spots of our

meta-device (see S12 of the Supplemental information). Experimental results indicate that the average scanning aberrations of our proposed dual-focus scanner for focal spots A and B are around 2.5% and 4.6% during the entire scanning process. The focusing efficiencies at $\Delta\alpha = 0°, 10°, 20°, 30°$ for focal spots A and B were 12.5%/11.8%, 12.6%/13.2%, 13.4%/12.7% and 12.2%/13.1%, respectively. A good agreement is noted between the experimental and theoretical predictions.

Conclusions

We propose and realize an innovative approach to achieve adaptive aberration corrections in coordination with the scanning of focal spot by cascaded metasurfaces. Our meta-devices are capable of correcting aberrations on any custom-designed curved surfaces, without any additional optical components and external interventions. By introducing three approximated phase functions, we simplified the design process into a deterministic phase-profile parameter searching algorithm. Based on such a design strategy, we successfully engineered, fabricated, and characterized two adaptively corrected meta-devices in the terahertz regime. The first meta-device is capable of dynamically scanning the focal spot on a planar surface with adaptively corrected scanning aberrations, while the second one scans two focal spots on two curved surfaces. In comparison to scanning lenses with hyperbolic or quadratic phase distributions, our design offers significant advantages in terms of flexibility in both surface shapes and the number of focal points (see S7 of the Supplemental information). Moreover, this method can be applied to other operating bands (such as near-infrared, and visible) by resizing the constituent building blocks (see S10 of the Supplementary information). However, maintaining precise alignment and minimizing spacing distance between the two metasurfaces at visible frequency may pose a significant experimental challenge. On other hand, our proposed meta-device can also be implemented in microwave regime, where the dielectric metasurface would be replaced with the multilayer metallic metasurfaces. Frequencies lower than microwave (such as the meter-wave band) would require metasurfaces that are excessively thick to fabricate effectively. Our research opens the gateway toward dynamic meta-devices capable of adaptive fine-tuning to meet high-precision demands, with potential applications in laser processing, lithography, and optical tweezers.

References

1. Marshall GF, Stutz GE. *Handbook of Optical and Laser Scanning*. (CRC Press, Boca Raton, 2004).
2. Guthoff RF, Baudouin C, Stave J. *Atlas of Confocal Laser Scanning In-vivo Microscopy in Ophthalmology*. (Springer, Berlin Heidelberg, 2007).
3. Yu NF, Genevet P, Kats MA et al. Light propagation with phase discontinuities: generalized laws of reflection and refraction. *Science* **334**, 333–337 (2011).
4. Sun SL, He Q, Xiao SY et al. Gradient-index meta-surfaces as a bridge linking propagating waves and surface waves. *Nat Mater* **11**, 426–431 (2012).
5. Yin XB, Ye ZL, Rho J et al. Photonic spin hall effect at metasurfaces. *Science* **339**, 1405–1407 (2013).
6. Lin RJ, Su VC, Wang SM et al. Achromatic metalens array for full-colour light-field imaging. *Nat Nanotechnol* **14**, 227–231 (2019).
7. Geng Q, Wang DE, Chen PF et al. Ultrafast multi-focus 3-D nano-fabrication based on two-photon polymerization. *Nat Commun* **10**, 2179 (2019).
8. Yang BW, Liu T, Guo HJ et al. High-performance meta-devices based on multilayer meta-atoms: interplay between the number of layers and phase coverage. *Sci Bull* **64**, 823–835 (2019).
9. Zhang F, Pu MB, Li X et al. Extreme‐angle silicon infrared optics enabled by streamlined surfaces. *Adv Mater* **33**, 2008157 (2021).
10. Qiu CW, Zhang T, Hu GW et al. Quo vadis, metasurfaces. *Nano Lett* **21**, 5461–5474 (2021).
11. Pan MY, Fu YF, Zheng MJ et al. Dielectric metalens for miniaturized imaging systems: progress and challenges. *Light Sci Appl* **11**, 195 (2022).
12. Guan FX, Guo XD, Zeng KB et al. Overcoming losses in superlenses with synthetic waves of complex frequency. *Science* **381**, 766–771 (2023).
13. Go GH, Park CH, Woo KY et al. Scannable dual-focus metalens with hybrid phase. *Nano Lett* **23**, 3152–3158 (2023).
14. Cui TJ, Qi MQ, Wan X et al. Coding metamaterials, digital metamaterials and programmable metamaterials. *Light Sci Appl* **3**, e218 (2014).
15. Chen K, Feng YJ, Monticone F et al. A reconfigurable active Huygens' metalens. *Adv Mater* **29**, 1606422 (2017).
16. Zhang L, Chen XQ, Liu S et al. Space-time-coding digital metasurfaces. *Nat Commun* **9**, 4334 (2018).
17. Casolaro A, Toscano A, Alù A et al. Dynamic beam steering with reconfigurable metagratings. *IEEE Trans Antennas Propag* **68**, 1542–1552 (2020).
18. Zhang XG, Jiang WX, Jiang HL et al. An optically driven digital metasurface for programming electromagnetic functions. *Nat Electron* **3**, 165–171 (2020).
19. Forouzmand A, Mosallaei H. A tunable semiconductor-based transmissive metasurface: dynamic phase control with high transmission level. *Laser Photon Rev* **14**, 1900353 (2020).
20. Venkatesh S, Lu XY, Saeidi H et al. A high-speed programmable and scalable terahertz holographic metasurface based on tiled CMOS chips. *Nat Electron* **3**, 785–793 (2020).
21. Li Y, Lin J, Guo HJ et al. A tunable metasurface with switchable functionalities: from perfect transparency to perfect absorption. *Adv Opt Mater* **8**, 1901548 (2020).
22. Hu YQ, Ou XN, Zeng TB et al. Electrically tunable multifunctional

polarization-dependent metasurfaces integrated with liquid crystals in the visible region. *Nano Lett* **21**, 4554–4562 (2021).

23. Kim J, Seong J, Yang Y et al. Tunable metasurfaces towards versatile metalenses and metaholograms: a review. *Adv Photonics* **4**, 024001 (2022).

24. Xu Q, Su XQ, Zhang XQ et al. Mechanically reprogrammable Pancharatnam-Berry metasurface for microwaves. *Adv Photonics* **4**, 016002 (2022).

25. Li QS, Cai XD, Liu T et al. Gate-tuned graphene meta-devices for dynamically controlling terahertz wavefronts. *Nanophotonics* **11**, 2085–2096 (2022).

26. Li C, Jang J, Badloe T et al. Arbitrarily structured quantum emission with a multifunctional metalens. *eLight* **3**, 19 (2023).

27. Qin JZ, Wang MJ, Qiu CW. Graphene metasurface hits the point. *Light Sci Appl* **12**, 110 (2023).

28. Badloe T, Kim Y, Kim J et al. Bright-field and edge-enhanced imaging using an electrically tunable dual-mode metalens. *ACS Nano* **17**, 14678–14685 (2023).

29. Xu HX, Ma SJ, Luo WJ et al. Aberration-free and functionality-switchable meta-lenses based on tunable metasurfaces. *Appl Phys Lett* **109**, 193506 (2016).

30. Bernet S, Ritsch-Marte M. Adjustable refractive power from diffractive moiré elements. *Appl Opt* **47**, 3722–3730 (2008).

31. Iwami K, Ogawa C, Nagase T et al. Demonstration of focal length tuning by rotational varifocal moiré metalens in an ir-A wavelength. *Opt Express* **28**, 35602–35614 (2020).

32. Cai XD, Tang R, Zhou HY et al. Dynamically controlling terahertz wavefronts with cascaded metasurfaces. *Adv Photonics* **3**, 036003 (2021).

33. Luo Y, Chu CH, Vyas S et al. Varifocal metalens for optical sectioning fluorescence microscopy. *Nano Lett* **21**, 5133–5142 (2021).

34. Liu S, Ma SJ, Shao RW et al. Moiré metasurfaces for dynamic beamforming. *Sci Adv* **8**, eabo1511 (2022).

35. Martins R J, Marinov E, Youssef M A B et al. Metasurface-enhanced light detection and ranging technology. *Nat Commun* **13**, 5724 (2022).

36. Ogawa C, Nakamura S, Aso T et al. Rotational varifocal moiré metalens made of single-crystal silicon meta-atoms for visible wavelengths. *Nanophotonics* **11**, 1941–1948 (2022).

37. Wei QS, Huang LL, Zhao RZ et al. Rotational multiplexing method based on cascaded metasurface holography. *Adv Opt Mater* **10**, 2102166 (2022).

38. Zhang JC, Wu GB, Chen MK et al. A 6G meta-device for 3D varifocal. *Sci Adv* **9**, eadf8478 (2023).

39. Zhang JC, Chen MK, Fan YB et al. Miniature tunable airy beam optical meta-device. *Opto-Electron Adv* **7**, 230171 (2024).

40. Kim J, Seong J, Kim W et al. Scalable manufacturing of high-index atomic layer–polymer hybrid metasurfaces for metaphotonics in the visible. *Nat Mater* **22**, 474–481 (2023).

41. Palmieri A, Dorrah AH, Yang J et al. Do dielectric bilayer metasurfaces behave as a stack of decoupled single-layer metasurfaces. *Opt Express* **32**, 8146–8159 (2024).

Acknowledgements

Author contributions

X. T. Li conducted the numerical simulations, performed the terahertz experiments, and prepared the original draft. X. D. Cai developed the theoretical model, analyzed the results, and prepared the original draft. C. Liu helped with the numerical simulations and manuscript preparation. X. T. Li, X. D. Cai, Y. Kim, T. Badloe, and H. H. Liu assisted in data and results analysis. S. Y. Xiao initiated the idea, revised the manuscript, and supervised the project with some input from J. Rho. All authors participated in the discussion and confirmed the final manuscript.

Competing interests

The authors declare no competing financial interests.

Supplementary information

Supplementary information for this paper is available at
https://doi.org/10.29026/oea.2024.240085

Scan for Article PDF